Evaluating Printability of Buried Native EUV Mask Phase Defects through a Modeling and Simulation Approach

Mihir Upadhyaya[1], Vibhu Jindal[2], Adarsh Basavalingappa[1], Henry Herbol[1], Jenah Harris-Jones[3], Il-Yong Jang[4], Kenneth A. Goldberg[5], Iacopo Mochi[5], Sajan Marokkey[6], Wolfgang Demmerle[6], Thomas V. Pistor[7] and Gregory Denbeaux[1]

[1]College of Nanoscale Science and Engineering, University at Albany, 255 Fuller Road, Albany, New York, 12203, USA

[2]SEMATECH, 257 Fuller Rd, Albany, NY 12203, USA

[3]Global Foundries , 400 Stone Break Extension, Malta, NY 12020, USA

[4]Samsung Electronics Co., 129 Samsung-ro Suwon-Si, Gyeonggi-Do 443-742, Korea

[5]Lawrence Berkeley National Laboratory, One Cyclotron Road, Berkeley, CA 94720, USA

[6]Synopsys, 700 East Middlefield Road, Mountain View, CA 94043, USA

[7]Panoramic Technology Inc., Burlingame, CA 94010, USA

ABSTRACT

The availability of defect-free masks is considered to be a critical issue for enabling extreme ultraviolet lithography (EUVL) as the next generation technology. Since completely defect-free masks will be hard to achieve, it is essential to have a good understanding of the printability of the native EUV mask defects. In this work, we performed a systematic study of native mask defects to understand the defect printability caused by them. The multilayer growth over native substrate mask blank defects was correlated to the multilayer growth over regular-shaped defects having similar profiles in terms of their width and height. To model the multilayer growth over the defects, a novel level-set multilayer growth model was used that took into account the tool deposition conditions of the Veeco Nexus ion beam deposition tool. The same tool was used for performing the actual deposition of the multilayer stack over the characterized native defects, thus ensuring a fair comparison between the actual multilayer growth over native defects, and modeled multilayer growth over regular-shaped defects. Further, the printability of the characterized native defects was studied with the SEMATECH-Berkeley Actinic Inspection Tool (AIT), an EUV mask-imaging microscope at Lawrence Berkeley National Laboratory (LBNL). Printability of the modeled regular-shaped defects, which were propagated up the multilayer stack using level-set growth model was studied using defect printability simulations implementing the waveguide algorithm. Good comparison was observed between AIT and the simulation results, thus demonstrating that multilayer growth over a defect is primarily a function of a defect's width and height, irrespective of its shape. This would allow us to predict printability of the arbitrarily-shaped native EUV mask defects in a systematic and robust manner.

Extreme Ultraviolet (EUV) Lithography VI, edited by Obert R. Wood II, Eric M. Panning,
Proc. of SPIE Vol. 9422, 94220Q · © 2015 SPIE · CCC code: 0277-786X/15/$18
doi: 10.1117/12.2175842

Downloaded From: http://proceedings.spiedigitallibrary.org/ on 03/23/2015 Terms of Use: http://spiedl.org/terms

INTRODUCTION

Extreme ultraviolet lithography (EUVL) is being developed as a promising candidate for high-volume semiconductor manufacturing for 16 nm half-pitch patterning and beyond [1-3]. EUVL makes use of masks that are reflective in nature and that consist of a low thermal expansion material, typically quartz, coated with a Mo/Si multilayer and a patterned absorber layer. In addition to EUV source and resist issues, preparation of defect-free masks is one of the top critical concerns for the launch of EUVL into high volume manufacturing (HVM) [2,3]. Buried defects namely pits, bumps and particles, in EUV masks are one of the main hurdles in the development of EUV lithography. These defects can either be on the mask substrate or can get embedded within the multilayer during the multilayer deposition process [4-6].

It is essential to have a good understanding of the growth behavior of Mo/Si bilayer structure on top of a defect in an EUV mask. The study of multilayer growth on defects helps to understand the total phase change and the effect of curvature change for a given defect profile under given deposition conditions. The net phase change adds to the intrinsic effect of the core defect and its influence on the growth of the multilayer stack during deposition. Therefore, identifying this influence is critical and would help in determining strategies to mitigate the printability of such defects by employing various techniques like defect smoothing [7], multilayer defect compensation technique [8], or using additional buffer layer [9], to name a few.

In this study, we wanted to develop a reliable method to estimate the printability of the native EUV mask substrate defects, given the AFM profile on the multilayer top. There have been studies that have looked at multilayer growth over programmed substrate defects using non-linear continuum growth models [10-13], and have attempted to predict the printability of native defects. However, a systematic study correlating the multilayer growth over native defects versus programmed defects, and showing the comparison between their printabilities has been lacking. Here, we have developed an approximate but relatively accurate method for investigating defect printability of arbitrarily-shaped native defects, both bump-type and pit-type, given their AFM profiles on top of the multilayer stack.

The most commonly used model, namely the non-linear continuum model or the Stearns model [14] used to simulate the multilayer growth over a defect, assumes the deposition and etch fluxes to be at near normal incidence to the mask surface (thereby ignoring the shadowing effects due to the defect), which is not the case in modern coating-deposition systems. The model used here is based on the level-set technique [15] and incorporates the deposition conditions, including the angular flux of atoms incident on the substrate, the chamber geometry, and deposition factors such as substrate and target angles, distances between source, target and substrate and the rotational speed of the substrate. Here, we will briefly discuss the workings of the level-set multilayer growth model, as developed for our tool, to simulate Mo/Si bilayer growth over the native defects. The details of the growth model have been discussed elsewhere [16,17]. In our previous work, [18,19] using level-set modeled multilayer growth over native defect shapes, we showed good comparison between through-focus aerial image intensities as obtained at AIT [20] and those obtained through defect printability simulations.

Downloaded From: http://proceedings.spiedigitallibrary.org/ on 03/23/2015 Terms of Use: http://spiedl.org/terms

The aim of our work here was to develop a systematic technique/methodology for the study of arbitrarily-shaped native mask defects, using just the modeling (of multilayer growth) and simulation (of defect printability) approach, thereby helping to reduce dependence on actinic review techniques for mask blank inspection.

CHARACTERIZATION OF NATIVE DEFECTS ON EUV MASK BLANKS

Once the multilayer deposition process on the mask substrate is complete, the mask blank is analyzed for defects using a Lasertec M7360 inspection tool, which uses light scattering as a means to detect defects present on the substrate surface. The defect locations are marked with the help of fiducials to easily locate the defects for AFM, TEM and AIT printability studies. AFM is performed at the defect locations to observe the defect profile on top of the mask blanks. The masks are then sent to LBNL to undergo inspection at the AIT where the aerial images of the defect sites are obtained. TEM cross-section studies are then performed to observe the multilayer deformations created by the defects. The defect profile at the substrate, obtained from the cross-section TEM, is used as one of the inputs into the multilayer growth model.

MULTILAYER GROWTH MODEL

The multilayer growth model, we developed [16,17], looks at the deposition conditions of the Veeco Instruments' Nexus low defect density (LDD) tool located in the SEMATECH cleanroom facility in Albany, New York. The tool consists of an ion source, Si, Mo and Ru targets, and an electrostatic chuck to hold the mask substrate. The schematic of the tool is shown in Figure 1. Ar ions extracted from the ion source strike the target liberating the atoms to be deposited. The sputtered atoms travel to the mask substrate where they deposited, creating the multilayer reflector. The mask substrate is electrostatically chucked to the mask fixture, which precisely positions the substrate relative to the target and rotates the substrate around its normal direction.

Downloaded From: http://proceedings.spiedigitallibrary.org/ on 03/23/2015 Terms of Use: http://spiedl.org/terms

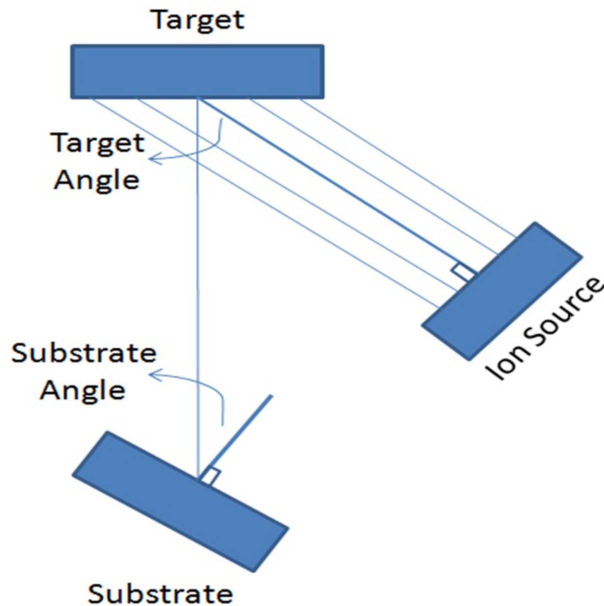

Figure 1: Top-down schematic of the Ion Beam Deposition tool.

The multilayer growth model uses the kinetic Monte Carlo method for calculating angular distribution of sputtered atom flux, and the level-set method for determining multilayer growth. The simulation method takes into account the flux of atoms sputtered from the target, the energy of the sputtered atoms, and gas scattering inside the chamber. It takes into account the probability of striking an ambient gas atom along the atom's trajectory and predicts the energy and direction of the atom after the collision. The scattering gas in the initial simulations was assumed to have a Boltzmann's velocity distribution at 50°C and to be comprised of argon atoms at 0.14 mTorr, which is the typical pressure inside the Veeco chamber during deposition. Modeling the deposition rate throughout the chamber requires estimates of several parameters, such as the number of atoms ejected from the target at each location on the target, which was estimated using measured target erosion profiles; the angular distribution of atoms reaching the substrate, which was estimated by measuring the deposition rate on substrates mounted on a hemispherical surface around the center of the target; the gas scattering behavior between the target and substrate, which was estimated using a kinetic Monte Carlo method and scattering cross sections. A collision kinetic theory with a random impact parameter was used to determine the post-collision velocity of the atom. The substrate rotation that is commonly used to improve uniformity in the Veeco Nexus tools is modeled by rotationally averaging the number of atoms that strike the substrate. The simulation results were validated by measuring deposition thickness from quartz crystal microbalances and wafer coupons placed at different places near substrate position. The details of the experimental and modeling results are reported elsewhere [16,17].

After determining the growth rates and uniformity on the multilayer, multilayer growth on a given defect profile can be simulated. The level-set method was used to simulate defect growth during multilayer deposition. Simulations of defect shape and growth during this deposition took into account the nature and profile of the defect (pit or bump) and direction and incident flux of

Downloaded From: http://proceedings.spiedigitallibrary.org/ on 03/23/2015 Terms of Use: http://spiedl.org/terms

the material, based on the deposition conditions. The initial defect profile at the mask substrate was defined using the cross-section TEM image through the defect.

SYSTEMATIC STUDY OF THE PRINTABILITY OF NATIVE EUV MASK DEFECTS

a. Correlating Multilayer Growth over Native Defects to that over Regular-shaped Defects

First, we wanted to establish a clear correlation between the defect profiles at the substrate and the resulting defect profiles at the top of the multilayer, for the given deposition conditions of our ion beam deposition tool, the Veeco Nexus. In a study conducted at SEMATECH by Il-Yong Jang et al. [21], AFM measurements of native defects were performed at the substrate (prior to multilayer deposition) as well as at the multilayer top, and a graph showing the substrate defect width versus the multilayer top defect width was obtained. 15 bump and 15 pit defects were characterized for this study. The native defects chosen for this study all had shallow heights (or depths), approximately equal to 3 nm. The reason why the shallow defects were characterized for this study was so that the height or depth of the defect did not have a significant impact on the propagation of defect width up the multilayer stack. For our simulation study, we used Gaussian-shaped substrate defects having various FWHMs and a height or depth of 3 nm, to be similar as the native defects used in the aforementioned study. We simulated multilayer growth over these defects using the level-set multilayer growth model and obtained the defect profiles on the multilayer top. We then plotted the multilayer top defect FWHM as a function of the substrate defect FWHM and compared this to results obtained by Jang et al. [21]. The comparison is shown in Figure 2. We observe a good comparison between the simulation (performed using Gaussian defect profiles) and experimental results (obtained for native defect profiles), thus showing that multilayer growth over a defect shape is primarily a function of its FWHM and height.

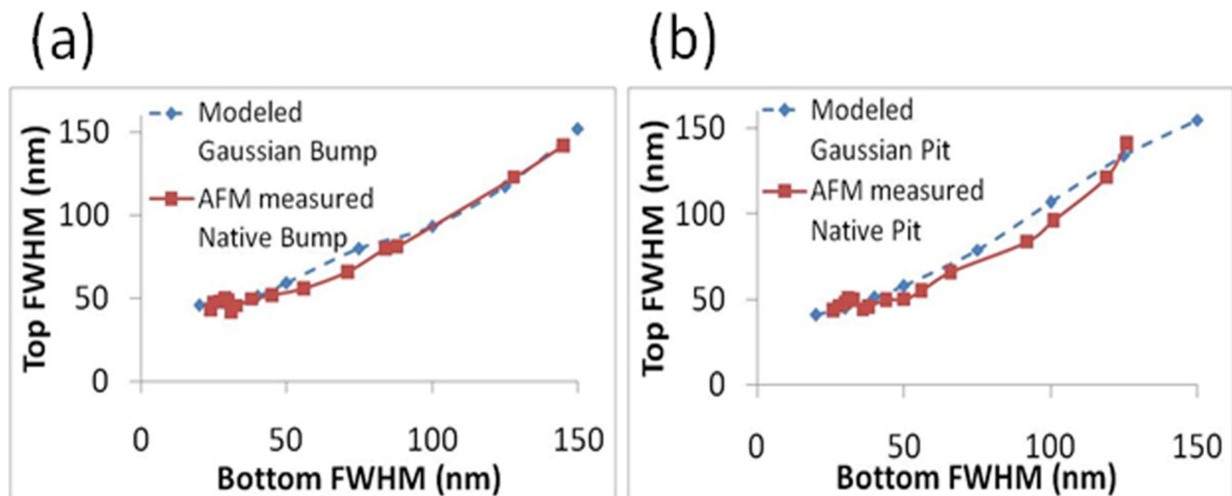

Figure 2: Defect FWHM on multilayer top as a function of substrate defect FWHM for (a) bump defect and (b) pit defect. Solid-line curve in the plot is as obtained by Jang et al. [21].

Since the experimental study had been performed using the Veeco Nexus IBD tool and our growth model was developed for that tool itself, we could draw a fair comparison between the

Downloaded From: http://proceedings.spiedigitallibrary.org/ on 03/23/2015 Terms of Use: http://spiedl.org/terms

experimental and our simulation results. The above result led us to hypothesize that irrespective of the arbitrary shape of the native defect, the first few bilayers deposited tend to smooth out any irregularities in the defect profile, and as a result the critical top bilayers also end up having a relatively smooth regular profile.

Next, proceeding with the assumption that multilayer growth over an arbitrarily-shaped defect is similar to that over a Gaussian-shaped defect having similar width and height at the substrate, we sought to map the defect profile at the top surface as a function of the substrate defect profile, for our deposition tool. For this, we simulated multilayer growth over Gaussian-shaped bump and pit defects using our level-set growth model. Multilayer growth over 25 Gaussian bump-type and 25 Gaussian pit-type defects was simulated to obtain the plots as shown in Figure 3. Figure 3(a) shows the top-surface FWHM as a function of the substrate defect FWHM and height for a Gaussian bump defect, and Figure 3(b) shows the top defect height as a function of the substrate defect FWHM and height for a Gaussian bump defect. Figure 3(c) shows the overlay of the two maps as shown in Figure 3(a) and Figure 3(b) in the form of a contour plot. Given the top FWHM and height of a bump defect (as determined by AFM scan), the contour plot can be used to determine the Gaussian-equivalent-FWHM-and-height (GEFH) of the defect at the substrate. Figure 3(c), Figure 3(d) and Figure 3(e) show the same information as Figure 3(a), Figure 3(b) and Figure 3(c) respectively, but for a Gaussian pit defect.

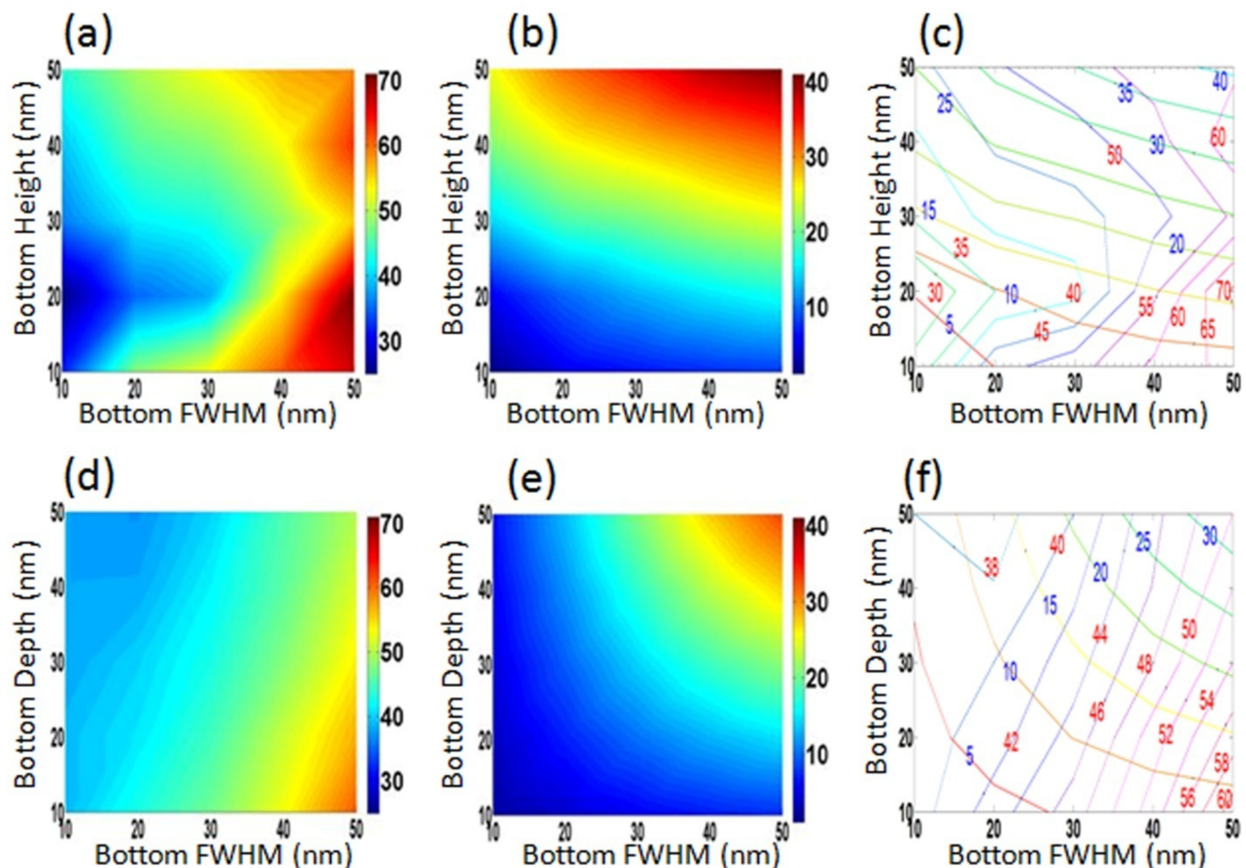

Figure 3: (a) Map of top defect FWHM and (b) map of top defect height as a function of bottom (substrate) FWHM and height of defect for Gaussian bump defect. (c) Contour plots showing top

Downloaded From: http://proceedings.spiedigitallibrary.org/ on 03/23/2015 Terms of Use: http://spiedl.org/terms

FWHM and top height as a function of substrate FWHM and height of defect for Gaussian bump defect. (d) Map of top defect FWHM and (e) map of top defect depth as a function of bottom (substrate) FWHM and depth of defect for Gaussian pit defect. (f) Contour plots showing top FWHM and top depth as a function of substrate FWHM and depth of defect for Gaussian pit defect.

So, given an AFM scan of a native defect at the top multilayer surface, we can now infer the buried substrate defect profile in terms of GEFH using the contour maps shown in Figure 3. Here, we must note that the maps (and the corresponding contour plots) shown in Figure 3 yield a unique solution to the bottom Gaussian-equivalent defect profile for a given top defect profile in most of the given parameter space. Starting with a Gaussian defect at the substrate (having FWHM and height as determined by GEFH obtained from the contour plots), we can simulate the multilayer growth over that defect using the level-set multilayer growth model, which would in turn be imported into defect printability simulation software to obtain a printability result in terms of the aerial image intensity. The underlying assumption for this approach is that the defect is present at the mask substrate, and not within the multilayer. This is a reasonable assumption since studies have shown that most of the buried defects are present at the mask substrate itself [22,23].

b. Comparing Printability Performance of Native, Gaussian, and Regular-shaped Substrate Defects

Next, we investigated the impact of FWHM and height of the defect on the defect printability (in terms of the aerial image intensity). For this, we identified two native, substrate EUV mask defects and compared their measured aerial image intensities (from the AIT) with simulated aerial image intensities.

Printability simulations were performed using a waveguide algorithm [24]. The optical and imaging parameters used for the simulations were chosen to match the parameters used for the AIT imaging, which were 13.5 nm wavelength radiation incident on the mask at an angle of 6 degrees, disk-fill illumination with a σ value of 0.2, and a mask-side numerical aperture (NA) of 0.0875 (0.35, 4x wafer-side).

Multilayer growth simulations were performed over three substrate defect profiles corresponding to each of the characterized native mask defects. First, multilayer growth was simulated over the native defect shapes obtained from cross-section TEM images as seen in Figures 4 and 5. Defect-shape outlines observed in cross-section TEM images are used as the input substrate defect shapes for the level-set growth model. Second, Gaussian substrate defect shapes were used as input into the multilayer growth model. We determined the FWHM and height of the characterized native defects at the multilayer top-surface using the AFM scans. The maps shown in Figure 3 were used to determine the GEFH of the defects at the substrate, which were then used as inputs into the multilayer growth model. Third, to demonstrate (as per our hypothesis in the previous section) that a truly arbitrarily-shaped defect can be completely defined just in terms of its FWHM and height for the purpose of predicting its printability, we simulated multilayer growth over defects that were rectangular in shape. FWHM and height values used for Gaussian

Downloaded From: http://proceedings.spiedigitallibrary.org/ on 03/23/2015 Terms of Use: http://spiedl.org/terms

defects were used for rectangular defects as well, except that FWHM that was used to define Gaussian defects simply translated into the width of the rectangle-shaped defects.

Figure 4(c) shows the comparison of the AIT aerial image intensity cross-sections for the pit native defect with the simulated aerial image intensities for the modeled native, Gaussian and rectangle-shaped defects. The modeled coating properties above the defects are shown in Figure 4(a). We observe a good match between the AIT and simulated aerial image intensities (for the rotationally symmetric simulated defect growths), with the AIT-to-modeled native contrast difference being equal to 1%, AIT-to-modeled Gaussian contrast difference equal to 3% and AIT-to-modeled rectangle contrast difference equal to 8%.

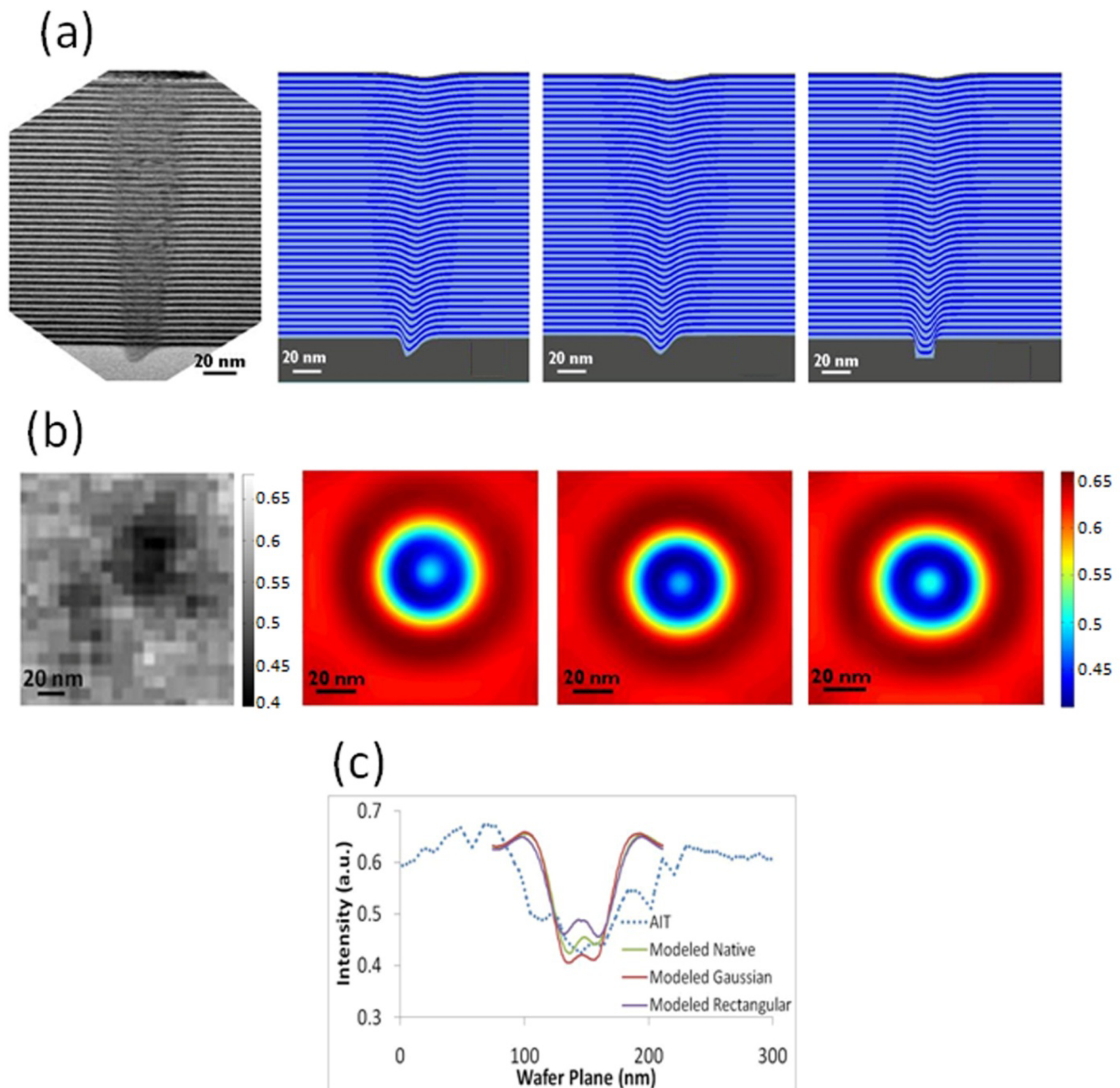

Figure 4: (a) Cross-section of native EUV mask defect, simulated native mask defect, simulated Gaussian mask defect and simulated rectangular mask defect (left to right), (b) corresponding 2-

Downloaded From: http://proceedings.spiedigitallibrary.org/ on 03/23/2015 Terms of Use: http://spiedl.org/terms

D aerial image intensity maps, and (c) aerial image intensity cross-section comparison between native defect and simulated defects. Defect printability simulations performed using waveguide algorithm.

Figure 5(c) shows the comparison of the AIT aerial image intensity cross-sections for the bump native defect with the simulated aerial image intensities for the modeled native, Gaussian and rectangle-shaped defects. The modeled coating properties above the defects are shown in Figure 5(a). We observe a good match between the AIT and simulated aerial image intensities (for the rotationally symmetric simulated defect growths), with the AIT-to-modeled native contrast difference being negligible, AIT-to-modeled Gaussian contrast difference equal to 1% and AIT-to-modeled rectangle contrast difference equal to 6%.

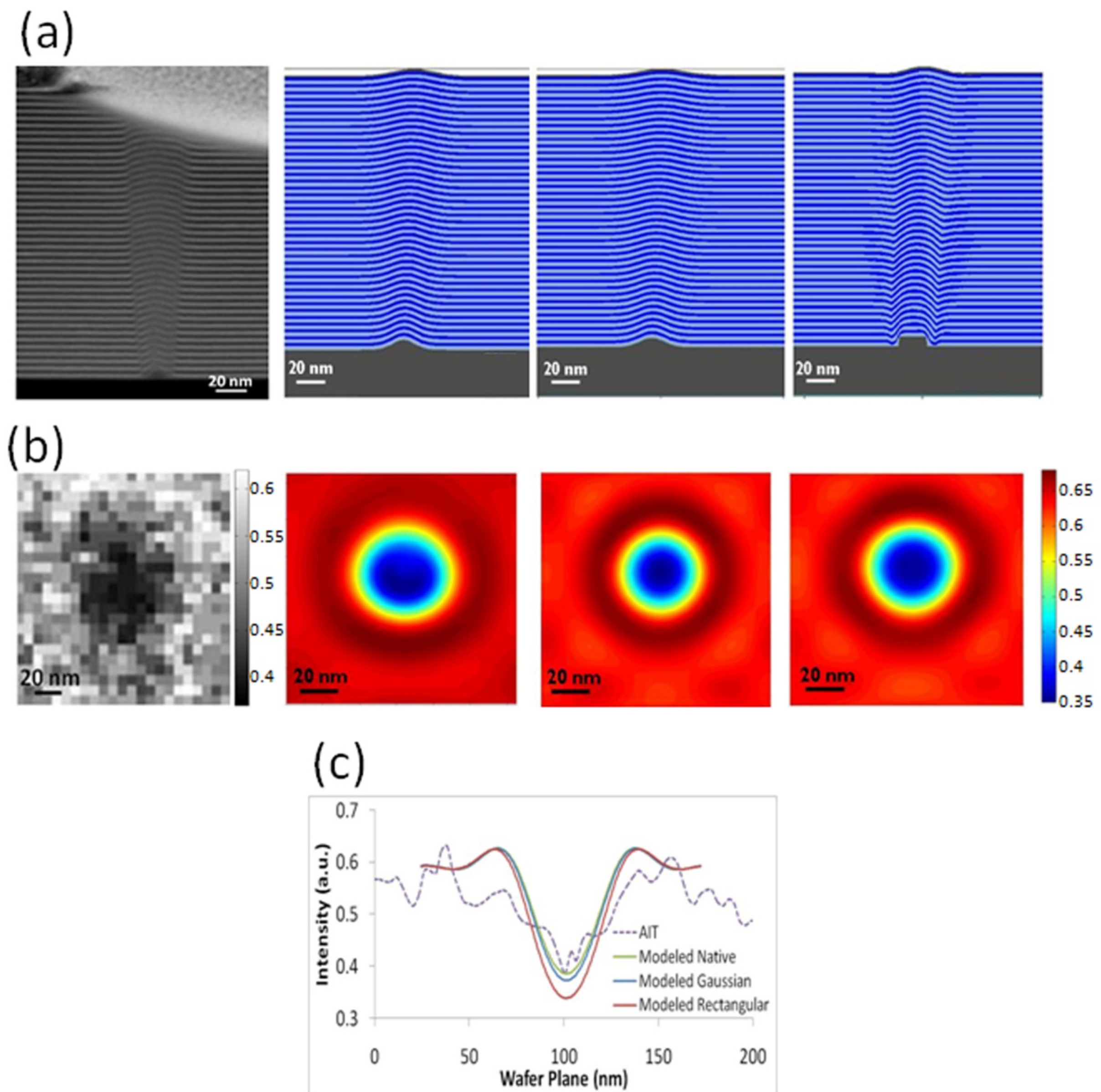

Figure 5: (a) Cross-section of native EUV mask defect, simulated native mask defect, simulated

Downloaded From: http://proceedings.spiedigitallibrary.org/ on 03/23/2015 Terms of Use: http://spiedl.org/terms

Gaussian mask defect and simulated rectangular mask defect (left to right), (b) corresponding 2-D aerial image intensity maps, and (c) aerial image intensity cross-section comparison between native defect and simulated defects. Defect printability simulations performed using waveguide algorithm.

The aerial image intensities shown in Figure 4 and Figure 5 are at best focus conditions i.e. defocus equal to zero. Here, we would like to make a note that we performed simulation studies [25] to look at the impact of defect (Gaussian-shaped) volume on aerial image contrast and observed a wide range of contrast values for the same defect volume, thus further demonstrating that both the width and height information of the defect is needed to fully characterize it in terms of predicting its printability behavior, and volume information alone is not sufficient, and can even be misleading.

Thus, we conclude that the critical top few layers of the multilayer are not much affected by the defect shape at the substrate with similar FWHM and heights, and evolve in a similar manner up the multilayer stack, thus resulting in similar printability performance. There have been studies that have correlated the clear field contrast of aerial image intensity due to a defect as observed by AIT to the printability caused by that defect in dense line and space (L/S) features under different imaging conditions [26,27]. Our aim through this study was to reduce the dependence on actinic review techniques for determining printability of defects.

c. Proposed Mask Fabrication Process Flow and Caveats

Here we propose a process flow to predict the aerial image contrast caused by native defects on EUV mask blanks, and consequently determine the likelihood of the defect printing on the wafer. Such an approach could save time and resources involved in the use of actinic review tool, as our approach relies on simulations and AFM measurements of defects found with DUV inspection. We propose a mask fabrication process flow as shown in Figure 6.

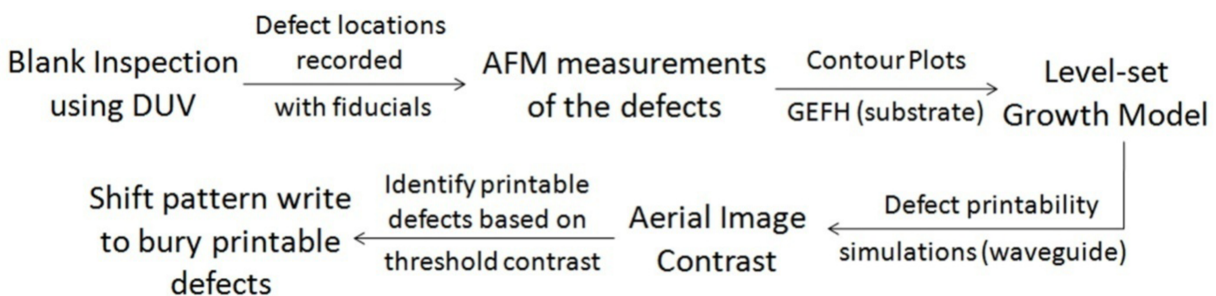

Figure 6: Proposed automated process flow for mask blank inspection.

The motivation behind the above study (and the resulting proposed process flow) is that an actinic blank review tool must be able to fully quantify the printability of each defect. All relevant defects on a blank need to be detected regardless of what they are. Their locations should be recorded and the effect of these defects on printability must be quantified. And finally, based on the above information, a decision must be made whether to discard or repair the mask, including consideration of smart pattern placement to cover some defects [28].

Downloaded From: http://proceedings.spiedigitallibrary.org/ on 03/23/2015 Terms of Use: http://spiedl.org/terms

The process flow proposed above comes with a caveat pertaining to the use of modeling and simulations for predicting defect printability. The 3-D defects simulated in this work to show comparison to AIT were assumed to be rotationally symmetric, while we know that the native defects can have arbitrary shapes. 3-D rotationally symmetric defects were assumed for both the level-set growth model as well as the defect printability simulations. Also, we have assumed for our studies that the defect is present at the mask substrate only. The above process flow would need to be adapted for defects embedded in the multilayer coating. However, we have stated that most of the buried phase defects occur at the substrate itself [22,23], thus allowing our model to be generally valid.

Finally, predicting the printability of a defect in the resist on the basis of simulated aerial image data can be challenging. There have been a number of studies that have looked at the printability of absorber pattern defects by fabricating programmed defects on test masks [29-32]. These studies showed that the resist printability results do not correlate too well with those from the aerial image simulations (based on a threshold model to determine CD change). These studies observed that resists can limit the printing of defects below a certain size owing to their limited resolution. Therefore simply performing the aerial image simulations is not sufficient to determine the true defect printability. Without a resist model, aerial images appear to overestimate defect printability, especially for smaller defects [31,32]. Therefore relying only on simulated aerial image intensities could lead to a conservative overestimate of the number of printable defects on a mask blank. The estimation of a certain threshold value of contrast of aerial image intensity for a defect in clear field as a criterion for defect printability has to somehow be convolved with the resist parameters, for different resists to get a more realistic estimate of the defect printability criterion for the different resists. Furthermore, the important interactions of buried defects with adjacent overlaying absorber patterns cannot be overlooked. Such interactions are difficult to generalize in the context of complex patterns and ever-shrinking design rules.

CONCLUSION

In this study, we compared the printability of native EUV mask substrate defects to that of similar-profiled regular-shaped defects. Using a multilayer growth model that took into account the tool deposition conditions where the multilayer coating took place, we simulated multilayer growth over regular-shaped substrate defects having similar profiles as those of native defects and found a good correlation between their widths at the substrate and on top of the multilayer. Also, a good comparison between simulated aerial image intensities for regular-shaped defects, and AIT aerial image intensities for native mask defects was obtained, for the native and regular-shaped defects having similar profiles. Therefore, we were able to show that a defect can be completely characterized in terms of its FWHM and height for the defect printability studies. With the information of the defect profile at the multilayer top (using AFM scan), the Gaussian-equivalent substrate defect profile can be inferred with the help of the top-to-substrate defect profile maps (Figure 3), and using the level-set multilayer growth model, the multilayer evolution over the defect from the substrate up can be obtained. We showed that native, Gaussian and rectangular substrate defect profiles having similar FWHMs (or widths in case of

Downloaded From: http://proceedings.spiedigitallibrary.org/ on 03/23/2015 Terms of Use: http://spiedl.org/terms

rectangle) and heights yield similar aerial image intensities. We finally proposed a process flow that could reduce our dependence on actinic imaging for qualifying EUV mask blanks.

ACKNOWLEDGMENTS

The authors would like to acknowledge the helpful ideas from Yudhishthir Kandel of SUNY College of Nanoscale Science and Engineering.

REFERENCES

[1] B. LaFontaine, Y. Deng, R.-H. Kim, H. J. Levinson, S. McGowan, U. Okoroanyanwu, R. Seltmann, C. Tabery, A. Tchikoulaeva, T. Wallow, O. Wood, J. Arnold, D. Canaperi, M. Colburn, K. Kimmel, C.-S. Koay, E. McLellan, D. Medeiros, S. P. Rao, K. Petrillo, Y. Yin, H. Mizuno, S. Bouten, M. Crouse, A. van Dijk, Y. van Dommelen, J. Galloway, S.-I. Han, B. Kessels, B. Lee, S. Lok, B. Niekrewicz, B. Pierson, R. Routh, E. Schmit-Weaver, K. Cummings and J. Word, "The use of EUV lithography to produce demonstration devices," *Proc. SPIE* **6921**, 69210P (2008).

[2] O. Wood, C.-S. Koay, K. Petrillo, H. Mizuno, S. Raghunathan, J. Arnold, D. Horak, M. Burkhardt, G. McIntyre, Y. Deng, B. La Fontaine, U. Okoroanyanwu, T. Wallow, G. Landie, T. Standaert, S. Burns, C. Waskiewicz, H. Kawasaki, J. H. C. Chen, M. Colburn, B. Haran, S. S. C. Fan, Y. Yin, C. Holfeld, J. Techel, J.-H. Peters, S. Bouten, B. Lee, B. Pierson, B. Kessels, R. Routh and K. Cummings, "EUV lithography at the 22nm technology node," *Proc. SPIE* **7636**, 76361M (2010).

[3] S. Wurm, C.-U. Jeon and M. Lercel, "SEMATECH's EUV program: A key enabler for EUVL introduction," *Proc. SPIE* **6517**, 651705 (2007).

[4] P. B. Mirkarimi and D. G. Stearns, "Investigating the growth of localized defects in thin films using gold nanospheres," *Appl. Phys. Lett.* **77**, 2243 (2000).

[5] R. V. Randive, A. Ma, P. A. Kearney, D. Krick, I. Reiss, P. B. Mirkarimi and E. Spiller, "Progress in the fabrication of low-defect density mask blanks for extreme ultraviolet lithography," *J. Microlith. Microfab. Microsyst.* **5**, 023003 (2006).

[6] Y. Lin and J. Bokor, "Minimum critical defects in extreme-ultraviolet lithography masks," *J. Vac. Sci. Technol. B* **15**, 2467 (1997).

[7] J. H-Jones, V. Jindal, P. Kearney, R. Teki, A. John and H.J. Kwon, "Smoothing of substrate pits using ion beam deposition for EUV lithography," *Proc. SPIE* **8322**, 83221S (2012).

[8] T. Liang and E. Gullickson, "Multilayer defect compensation to enable quality masks for EUV production," *International Symposium on EUV Lithography*, Lake Tahoe, California, 2008.

Downloaded From: http://proceedings.spiedigitallibrary.org/ on 03/23/2015 Terms of Use: http://spiedl.org/terms

[9] B.T. Lee, E. Hoshino, M. Takahashi, T. Yoneda, H. Yamanashi, H. Hoko, A. Chiba, M. ito, M. Ryoo, T. Ogawa and S. Okazaki, "Characteristics of the Ru buffer layer for EUVL mask patterning," *Proc. SPIE* **4343**, 746 (2001).

[10] H.J. Kwon, J. Harris-Jones and A. Cordes, M. Satake, Y. Li, I. Mochi and K.A. Goldberg, "EUV mask multilayer defects and their printability under different multilayer deposition conditions," *Proc. SPIE* **8322**, 832209 (2012).

[11] H.S. Seo, B.S. Ahn, I.Y. Kang, D.G. Lee, S. Huh, B. Cha, D. Kim, S.S. Kim, H.K. Cho and K.A. Goldberg, "Effects of multilayer deposition on the EUV printability and DUV inspectability of substrate pit defects," *International Symposium on EUV Lithography*, Prague, Czech Republic, October 18-21, 2009.

[12] I.Y. Kang, H.S. Seo, B.S. Ahn, D.G. Lee, D. Kim, S. Huh, C.W. Koh, B. Cha, S.S. Kim, H.K. Cho, I. Mochi and K.A. Goldberg, "Printability and inspectability of programmed pit defects on the masks in EUV lithography," *Proc. SPIE* **7636**, 76361B (2010).

[13] T. Liang, E. Ultanir, G. Zhang, S.J. Park, E. Anderson, E. Gullikson, P. Naulleau, F. Salmassi, P. Mirkarimi, E. Spiller and S. Baker, "Growth and printability of multilayer phase defects on EUV mask blanks," *International Symposium on EUV Lithography*, Sapporo, Japan, 2007.

[14] D.G. Stearns, P.B. Mirkarimi and E. Spiller, "Localized defects in multilayer coatings," *Thin Solid Films* **446**, 37 (2004).

[15] S.J. Osher and R. P. Fedkiw, "Level set methods and dynamic implicit surfaces," (Springer, New York), Vol. 153, 2003.

[16] T. Cardinal, D. Andruczyk, H. Yu, V. Jindal, P. Kearney and D. Ruzic, "Modeling the ion beam target interaction to reduce defects generated by ion beam deposition," *Proc. SPIE* **8322**, 8322Q (2012).

[17] V. Jindal, P. Kearney, J. Harris-Jones, A. Hayes and J. Kools, "Modeling the EUV Multilayer Deposition Process on EUV Blanks," *Proc. SPIE* **7969**, 79691A (2011).

[18] M. Upadhyaya et al., "Investigating printability of native defects on EUV mask blanks through simulations and experiments," *International Symposium on EUV Lithography*, Washington D.C., October 27 – 29, 2014.

[19] M. Upadhyaya et al., "Level-set multilayer growth model for predicting printability of buried native EUV mask defects," *J. Vac. Sci. Technol. B* **33**, 021602 (2015).

[20] K.A. Goldberg, I. Mochi, P. Naulleau, T. Liang, P.-Y. Yang, S. Huh, "EUV pattern defect detection sensitivity based on aerial image linewidth measurements," *J. Vac. Sci. Technol. B* **27** (6), 2916–21 (2009).

Downloaded From: http://proceedings.spiedigitallibrary.org/ on 03/23/2015 Terms of Use: http://spiedl.org/terms

[21] I.Y. Jang, R. Teki, V. Jindal, F. Goodwin, M. Satake, Y. Li, D. Peng, S. Huh and S.S. Kim, "Defect printability comparing actinic printing with advanced simulation for EUV masks," *Proc. SPIE* **8679**, 86790H (2013).

[22] V. Jindal, A. John, J. Harris-Jones, P. Kearney, A. Antohe and E. Stinzianni, "Inspection and compositional analysis of sub-20 nm EUV mask blank defects by thin film decoration technique," *Proc. SPIE* **8679**, 86791O (2013).

[23] A. Rastegar and V. Jindal, "EUV mask defects and their removal," *Proc. SPIE* **8352**, 83520W (2012).

[24] K.D. Lucas, H. Tanabe and A.J. Strojwas, "Efficient and rigorous three-dimensional model for optical lithography simulation," *J. Opt. Soc. Am. A* **13**, 2187 (1996).

[25] M. Upadhyaya, "Experimental and simulation studies of printability of buried EUV mask defects and study of EUV reflectivity loss mechanisms due to standard EUV mask cleaning processes," Ph.D. dissertation, State University of New York at Albany, pp. 103 – 104, 2014.

[26] S. Huh, A. Rastegar, S. Wurm, K.A. Goldberg, I. Mochi, T. Nakajima, M. Kishimoto and M. Komakine, "Study of real defects on EUV blanks and a strategy for EUV mask inspection," *Proc. SPIE* **7545**, 75450N (2010).

[27] S. Huh, P. Kearney, S. Wurm, F. Goodwin, H. Han, K. Goldberg, I. Mochi and E. Gullikson, "EUV actinic defect inspection and defect printability at the sub-32 nm half-pitch," *25th European Mask and Lithography Conference*, Dresden, Germany, Hanuary 12 – 15, 2010.

[28] P.Y. Yan, Y. Liu, M. Kamma, G. Zhang, R. Chen and F. Martinez, "EUVL multilayer mask blank defect mitigation for defect-free EUVL mask fabrication," *Proc. SPIE* **8322**, 83220Z (2012).

[29] Y. Tezuka, J. Cullins, Y. Tanaka, T. Hashimoto, I. Nishiyama and T. Shoki, "EUV exposure experiment using programmed multilayer defects for refining printability simulation," *Proc. SPIE* **6517**, 65172M (2007).

[30] Z. Zhang and T. Liang, "Investigation of resist effects on EUV mask defect printability," *Proc. SPIE* **6730**, 673016 (2007).

[31] T. Liang, G. Zhang, P. Naulleau, A. Myers, S. Park, A. Stivers and G. Vandentop, "EUV mask pattern defect printability," *Proc. SPIE* **6283**, 62830K (2006).

[32] C. Holfeld, K. Bubke, F. Lehmann, B. Fontaine, A. Pawloski, S. Schwarzl, F. Kamm, T. Graf, and A. Erdmann, "Defect printability study using EUV lithography," *Proc. SPIE* **6151**, 61510U (2006).

Downloaded From: http://proceedings.spiedigitallibrary.org/ on 03/23/2015 Terms of Use: http://spiedl.org/terms